

Observation of Cluster Magnetic Octupole Domains in the Antiferromagnetic Weyl Semimetal Mn_3Sn Nanowire

Hironari Isshiki^{1,2,*}, Nico Budai¹, Ayuko Kobayashi¹, Ryota Uesugi¹,
Tomoya Higo^{1,2,3}, Satoru Nakatsuji^{1,2,3,4} and YoshiChika Otani^{1,2,4,5}

¹*Institute for Solid State Physics, The University of Tokyo, Kashiwa, Chiba 277-8581, Japan*

²*CREST, Japan Science and Technology Agency (JST), Saitama 332-0012, Japan*

³*Department of Physics, The University of Tokyo, Bunkyo-ku, Tokyo 113-0033, Japan*

⁴*Trans-scale Quantum Science Institute, The University of Tokyo, Bunkyo-ku, Tokyo 113-0033, Japan*

⁵*Center for Emergent Matter Science RIKEN, Wako, Saitama 51-0198, Japan*



(Received 11 December 2023; accepted 19 April 2024; published 23 May 2024)

The antiferromagnetic Weyl semimetal Mn_3Sn has attracted wide attention due to its vast anomalous transverse transport properties despite barely any net magnetization. So far, the magnetic properties of Mn_3Sn have been experimentally investigated on micrometer scale samples but not in nanometers. In this study, we measured the local anomalous Nernst effect of a (0001)-textured Mn_3Sn nanowire using a tip-contact-induced temperature gradient with an atomic force microscope. Our approach directly maps the distribution of the cluster magnetic octupole moments with 80 nm spatial resolution, providing crucial information for integrating the Mn_3Sn nanostructure into spintronic devices.

DOI: [10.1103/PhysRevLett.132.216702](https://doi.org/10.1103/PhysRevLett.132.216702)

The antiferromagnetic Weyl semimetals Mn_3X ($X = \text{Sn, Ge}$) with a noncollinear spin structure in a kagome lattice have been drawing significant attention since they exhibit anomalous Hall and anomalous Nernst effects (ANE), which are generally absent in antiferromagnets [1–4]. The cluster magnetic octupole moment [5] in Mn_3X characterizes the momentum-space Berry curvature [6–8], which behaves as a macroscopic order parameter, like a ferromagnetic moment. These functional antiferromagnets hardly exhibit magnetic shape anisotropy due to their negligibly small demagnetizing fields [9]. This property will bring shape diversity into spintronic devices. For instance, nanowires must be magnetized along the wire-width direction in thermoelectric generation and heat flux sensing using an anomalous Nernst thermopile structure with a vertical temperature gradient [9–12]. With ferromagnetic nanowires, due to the shape anisotropy, we have to apply a finite external magnetic field along the wire-width direction for efficient voltage generation by the ANE. In contrast, when utilizing antiferromagnetic materials like Mn_3X , the negligible demagnetizing field enables this without an external magnetic field [9,13]. The efficiency and the stability of spintronic devices based on such antiferromagnets relies on the controllability of the octupole moments in nanostructures. Therefore, observing the octupole moments in a nanostructure is crucial for the practical application of Mn_3Sn .

This Letter presents the first demonstration of visualizing the spatial distribution of the cluster magnetic octupole moments within a (0001)-oriented polycrystalline Mn_3Sn nanowire. We employ a recently developed method based

on conventional atomic force microscopy (AFM) [14,15]. This technique involves establishing a tip-to-sample contact where the sample is heated, inducing a localized temperature gradient [16,17], and measuring the thermoelectric voltages due to the ANE at the wire's ends [17], as illustrated in Figs. 1(a) and 1(b). Thus, unlike the stray field measurements with the nitrogen-vacancy center magnetometry [18,19], our signals directly reflect the orientation of the local octupole moments. Similar methods that induce temperature gradients by lasers have been applied to the films and microwires of the Mn_3Sn [20,21], as well as magneto-optical Kerr effect measurements [22–24]. However, these measurements suffer from low spatial resolutions, whereas our technique maps in a resolution of 80 nm and is, therefore, more suitable for investigating nanowires.

We employed a dc magnetron sputtering method for growing a (0001)-textured polycrystalline Mn_3Sn film on a $\text{Si}(380\text{ nm})/\text{SiO}_2(500\text{ nm})$ substrate [9]. The 50-nm-thick Mn_3Sn film is sputtered from a $\text{Mn}_{2.7}\text{Sn}$ alloy target using a sputtering power of 60 W and an Ar gas pressure of 0.8 Pa. After the deposition, the film is transferred to the annealing chamber and annealed at 723 K for 30 mins in vacuum ($< 1 \times 10^{-6}$ Pa). Finally, a 2-nm-thick Al layer was deposited, which becomes an AlO_x layer after exposing to atmosphere and acts as a capping layer to prevent the oxidation of the Mn_3Sn . Scanning electron microscope-energy dispersive x-ray spectroscopy reveals that the composition of the film is $\text{Mn}_{3.12(2)}\text{Sn}_{0.88(2)}$, which is in the range where $\text{D}_{019}\text{Mn}_3\text{Sn}$ is reported to be stable [1,25]. Moreover, this Mn-rich condition is expected to promote

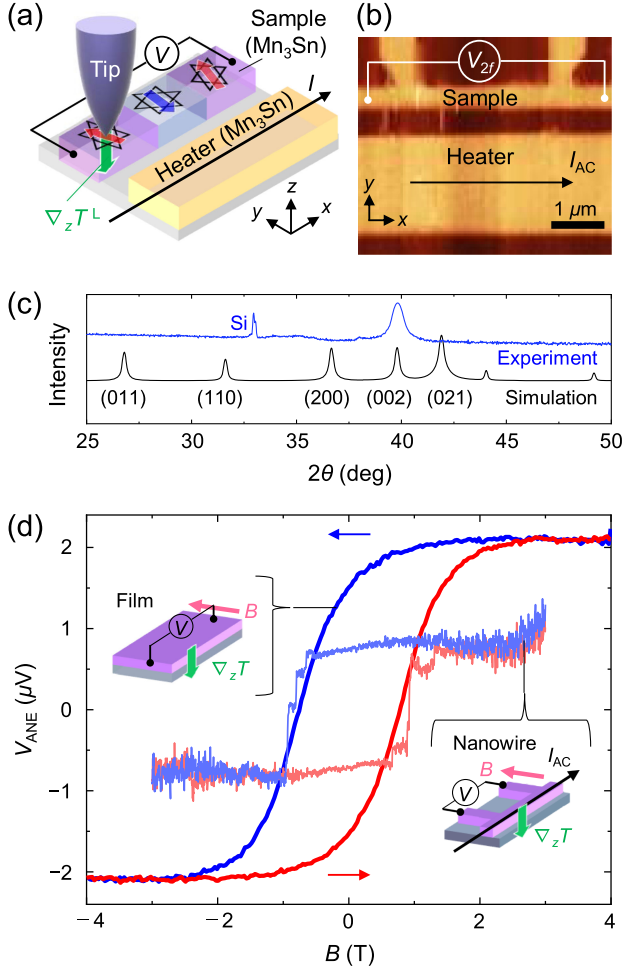


FIG. 1. Concept of our experiment and the basic properties of the Mn_3Sn . (a) Conceptual illustration of the experiment. (b) Topography of the whole device consisting of the sample and heating wires including the measurement configuration. (c) X-ray diffraction patterns of the Mn_3Sn film. The simulation is shown by the black curve. (d) Anomalous Nernst voltages of the film and nanowire as the function of the external magnetic field at room temperature.

the (0001)-preferred orientation of the Mn_3Sn layer [9]. The result of the $\theta - 2\theta$ scan of the x-ray diffraction for the films is shown in Fig. 1(c). We confirmed the single peak of (002) for the Mn_3Sn layer, which indicates that most of the kagome planes are parallel to the substrate, i.e., the (0001)-textured Mn_3Sn layer. We estimated the crystal grain size to be 100–250 nm [9,19] from a cross-sectional TEM measurement.

We used the (0001)-textured Mn_3Sn for the experiment below. Two parallel Mn_3Sn wires were fabricated by electron beam lithography and Ar ion etching for the AFM experiments. One serves as the sample wire, 400 nm in width, and the other is a 1.9- μm -wide heating wire. Their edge-to-edge separation is 600 nm. An AFM image of the device is shown in Fig. 1(b). We used an

atomic force microscope CoreAFM from Nanosurf [26] with a silicon cantilever Tap190Al-G (spring constant = 48 Nm^{-1}). Our device was placed on a homemade sample holder with a terminal for electrodes. We applied an alternating current (ac) to the heating wire with a frequency f . Joule heating increases the temperature of the sample wire by approximately 7 K, exhibiting oscillations at a frequency of $2f$. Very high frequency such as $f = 1$ MHz should not be used in this experiment since the temperature change would not saturate in the timescale of $2f$. Here, we chose $f = 1043.43$ Hz, which provides sufficient time for the heat to distribute thoroughly in the sample and still allows for a fast measurement by the lock-in amplifier. We scanned the tip at the sample surface in contact mode with a loading force of 50 nN. The resulting tip-contact-induced thermoelectric voltages (V_{2f}) across the sample wire were detected using the standard lock-in technique. We acquired both AFM topography and a voltage V_{2f} map simultaneously. The details of this technique are described in our previous works [14,15]. All measurements were performed in atmosphere at room temperature.

Initially, to confirm the behavior of the magnetic cluster octupole moments under in-plane magnetic field, we measured the ANE for the Mn_3Sn thin film before processing (5.2 mm \times 2 mm \times 50 nm) and its fabricated nanowire (3 μm \times 275 nm \times 50 nm: one similar to that for the AFM measurement) at 300 K. The results are shown in Fig. 1(d), including the measurement configurations for both devices. For the film, the temperature gradient (the magnetic field) was applied in the direction perpendicular (parallel) to the film using the method reported in the previous works [9,27]. We adopted the method recently developed by Leiva *et al.* [28] for the nanowire. An alternating current $I_{ac} = 0.2$ mA ($j_c = 1.3 \times 10^{10}$ A/m) was applied to the nanowire, which induces the out-of-plane temperature gradient in the whole wire, and the anomalous Nernst voltage was lock-in detected as the second harmonic signal. One can see the saturation of the signals at ~ 1 T with 0.78 μV for the nanowire. The hysteresis loop of the nanowire exhibits a well-defined remanent magnetization along the wire-width direction, indicating that the material retains a significant level of magnetization even in the absence of the external field. The abrupt switching at the smaller magnetic field reflects that the nanowire contains much fewer numbers of grains than the film. In these measurements, the magnitude of the anomalous Nernst voltage V_{ANE} is given by

$$V_{ANE} = l \cdot S_{ANE} \cdot \nabla_z T, \quad (1)$$

where l is the length of the sample, S_{ANE} is the coefficient for the ANE. According to the simulation using COMSOL Multiphysics, the temperature of the nanowire is increased by ~ 4 K, which results in vertical induced temperature gradient $\nabla_z T \sim 1.4 \times 10^6$ K/m. The value of S_{ANE} for the

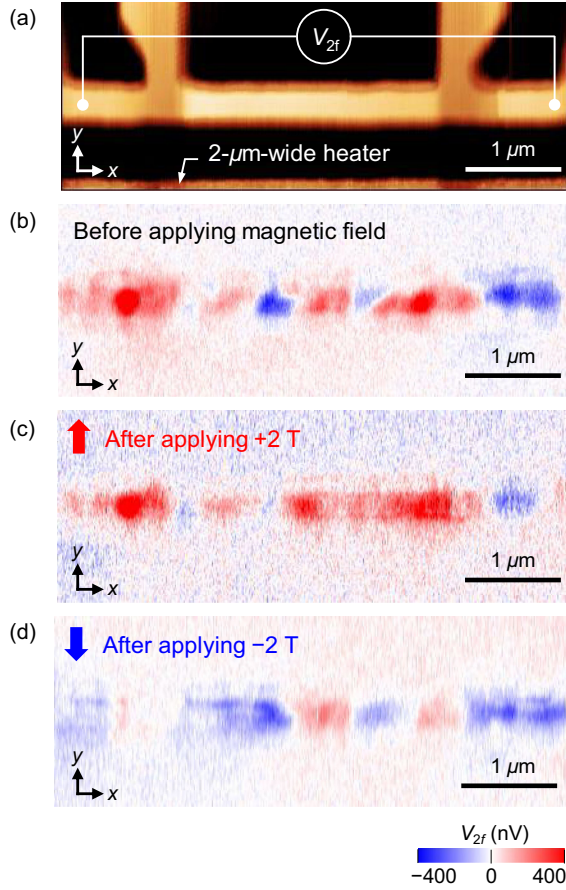


FIG. 2. Thermoelectric voltage mapping on the Mn_3Sn sample wire. (a) Magnified topography of the Mn_3Sn sample wire. (b) The local thermoelectric voltage mapping on the Mn_3Sn wire before applying an external magnetic field. (c),(d) The same, but after applying positive and negative 2 T along the y direction, respectively. The scanning areas for (a)–(d) are identical: the scan range is $5.4 \mu\text{m} \times 2.0 \mu\text{m}$ (400 pixels \times 150 pixels).

nanowire is estimated to be $0.18 \mu\text{V/K}$, nearly consistent with the one obtained in our previous works [9,29].

We show a magnified AFM image of the sample wire and the corresponding V_{2f} map before applying an external magnetic field in Figs. 2(a) and 2(b), respectively. To obtain Fig. 2(b), we applied $I_{ac} = 3.4 \text{ mA}$ ($j_c = 3.6 \times 10^{10} \text{ A/m}$) to the heating wire. We set $V_{2f} = 0 \text{ V}$ at the substrate in Fig. 2(b) to remove the offset. The signal V_{2f} at the sample wire is partially attributable to the local ANE in the textured Mn_3Sn sample. The tip contact with the sample surface induces a local out-of-plane temperature gradient $\nabla_z T^L$. The detectable anomalous Nernst voltage V_{ANE}^L along the wire-length direction is given by

$$V_{ANE}^L = \frac{1}{wt} \iiint S_{ANE} \cdot m_y \cdot \nabla_z T^L dx dy dz, \quad (2)$$

where m_y is the unit vector of the cluster magnetic octupole y component; w and t are the width and the thickness of the

nanowire, respectively. The range of integral is the volume near the tip where the out-of-plane temperature gradient extends. In our measurement configuration, the contributions of the in-plane temperature gradients to the ANE are negligible since the magnitude of the x component ($\nabla_x T^L$) is less than 2% of $\nabla_z T^L$ according to the simulation and the y component ($\nabla_y T^L$) does not produce anomalous Nernst voltage along the wire-length direction. The tip contact also induces a local temperature change ΔT^L , that causes the Seebeck effect (SE) [15,30,31] at, for example, grain boundaries where the Seebeck coefficient discontinuously changes. Ignoring the spatial resolution, the Seebeck voltage V_{SE}^L is given by

$$V_{SE}^L = (S_{xx}^{(A)} - S_{xx}^{(B)}) \cdot \Delta T^L, \quad (3)$$

where $S_{xx}^{(A)}$ and $S_{xx}^{(B)}$ are the Seebeck coefficients of adjacent two grains. Therefore, the signal shown in Fig. 2(b) results from the local ANE and SE.

To observe the magnetic response of the Mn_3Sn , we employed a magnetizing process along the $\pm y$ direction. The sample was positioned within an independent electromagnet, allowing us to control the magnetic field in the range of $\pm 2 \text{ T}$. We smoothly swept the magnetic field strength from 0 to 2 T in the positive or negative y directions, subsequently returning it to 0 T. After the application of the magnetic field, we repositioned the sample back into the AFM at its original location. We then repeated the V_{2f} mapping procedure at 0 T. The resulting V_{2f} mappings after applying $\pm 2 \text{ T}$ are represented in Figs. 2(c) and 2(d), respectively. Notably, following the application of a positive (negative) magnetic field, we observed an expansion of the areas displaying positive (negative) V_{2f} signals. This clearly illustrates the presence of a magnetic component within our signal.

We can numerically separate the magnetic (ANE) and nonmagnetic (SE) signals from Figs. 2(c) and 2(d) by having the following assumption: As magnetizing oppositely, the individual magnetic octupole moments reverse the direction while the positions of the magnetic domain boundaries remain unchanged [18,19]. This assumption can be verified by the ANE measurement for the nanowire shown in Fig. 1(d). Since the nonmagnetic SE signal is unchanged between the positively and negatively magnetized sample, the average and half difference between the V_{2f} in Figs. 2(c) and 2(d) give the SE and ANE signals, respectively. The results are shown in Figs. 3(a) and 3(b). We also subtract the nonmagnetic signals in Fig. 3(a) from the V_{2f} in Fig. 2(d), as shown in Fig. 3(c), which should indicate the ANE signal in the initial magnetic state. In Fig. 3(d), we show the line profile of the V_{SE} and V_{ANE} signals on the dashed lines in Figs. 3(a)–3(c). We will discuss the details in Fig. 3 after showing the simulation of the temperature distribution change induced by the tip.

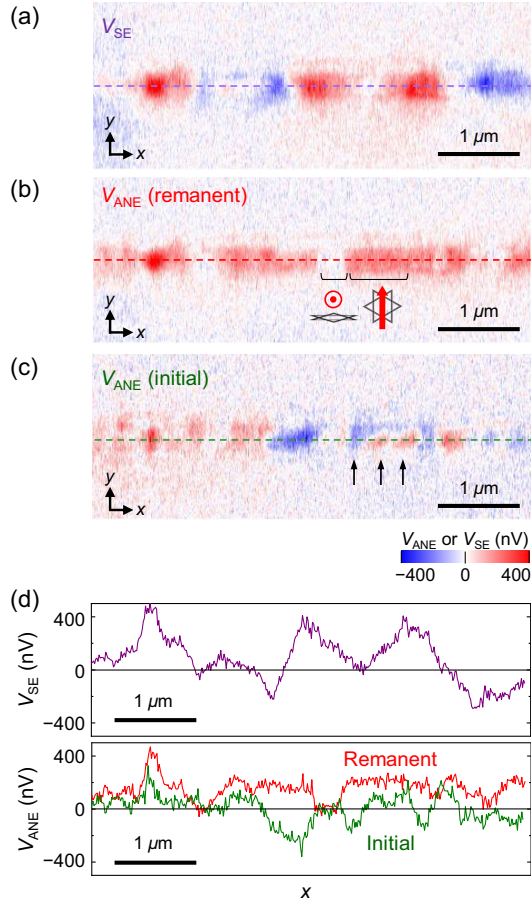


FIG. 3. Numerically extracted nonmagnetic and magnetic signals. (a) Nonmagnetic signal. (b) Magnetic signal after applying 2 T. (c) Magnetic signal in the initial state. The averaging and subtraction between the signals in Figs. 2(b)–2(d) produce these images. The numerical processing was performed after carefully aligning the shift of scanning positions. (d) The line profiles on the dashed lines in (a)–(c). The green and red profiles represent the magnetic signals before and after applying 2 T.

The results on another Mn_3Sn device shown in the Supplemental Material [32] are quantitatively very similar to Figs. 2(b)–2(d) and 3(a)–3(c).

For discussion on the quantitative thermoelectric coefficients and the spatial resolution of our technique, we need the temperature distribution induced by the tip contact in the sample wire. We performed numerical simulations on the geometry of our real device by using COMSOL Multiphysics [33]. According to studies in scanning thermal microscopy [34–36], the dominant heat transfer mechanisms between the tip and the sample are air conduction and water meniscus [37]. In our model, these mechanisms are represented by a disc-shaped virtual material inserted in between the tip and sample with phenomenological parameters: the thermal conductance $G_c = 20 \mu\text{W/K}$ and the contact thermal radius $r_c = 30 \text{ nm}$ (which should be comparable to the tip radius $> 10 \text{ nm}$) [15]. The heat conductivities of Mn_3Sn , Si (tip and substrate), and SiO_2

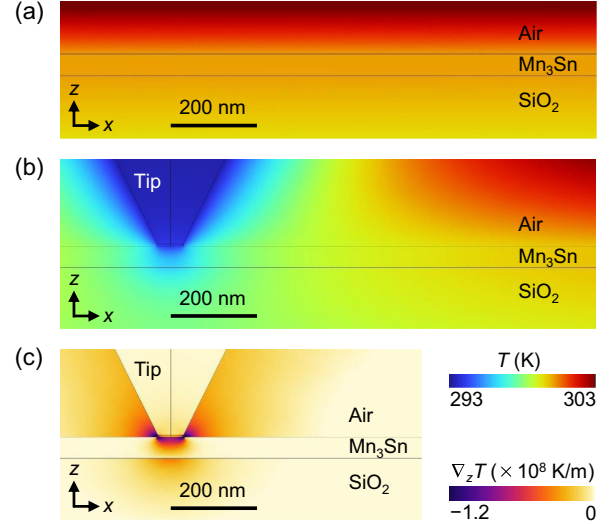


FIG. 4. Simulated temperature distribution of the Mn_3Sn sample wire by COMSOL Multiphysics. (a) Temperature distribution in the $x-z$ plane without tip contact. (b) Temperature distribution with tip contact. (c) Distribution of the out-of-plane temperature gradient with tip contact. The same geometry as the actual device has been set. The heating wire is behind the sample (Mn_3Sn) wire.

are 12 [38,39], 130 [40], and $1.2 \text{ W m}^{-1} \text{ K}^{-1}$ [41], respectively. We set the initial temperature to 293.15 K and applied a current of 3.4 mA ($j_c = 3.6 \times 10^{10} \text{ A/m}$) to the heating wire next to the sample. We omitted the surface oxide layer on top of the sample wire in the modeling, that barely affects the results of the simulation. The simulated results are shown in Figs. 4(a) and 4(b), the temperature distribution in the $x-z$ plane across the sample wire with and without tip contact, respectively. Before the tip contact, the temperature of the sample wire is $\sim 299 \text{ K}$, which is homogeneous, as shown in Fig. 4(a). The tip contact drastically changes the landscape of the temperature distribution as shown in Fig. 4(b). The temperature change ΔT^L ($\sim 1.2 \text{ K}$ on the average in the sample) extent of $\sim 500 \text{ nm}$ along the x direction. The out-of-plane temperature gradient $\nabla_z T^L$ with tip contact in the same plane is shown in Fig. 4(c). Remarkably, the out-of-plane temperature gradient is produced very locally: the extent in the x direction is $\sim 80 \text{ nm}$. Therefore, The integral in Eq. (2) should be taken in a cylindrical region with the radius of 80 nm in the Mn_3Sn sample (the magnitude of $\nabla_z T^L$ is $\sim 4 \times 10^6 \text{ K/m}$ on average in the cylindrical region). We found that the resolution of ANE ($\sim 80 \text{ nm}$) is much better than that of SE ($\sim 500 \text{ nm}$) in our technique, that is consistent to our previous experiments [14,15].

Figures 3(b) and 3(c) represent the distributions of the y -component of the cluster magnetic octupole moments in the Mn_3Sn nanowire with a spatial resolution of 80 nm. As shown in Fig. 3(c), the V_{ANE} becomes positive or negative depending on the position, which implies the randomly

distributed octupole domains in the initial state. Small islands of V_{ANE} marked by black arrows in Fig. 3(c) are attributable to grains of Mn_3Sn . After applying a magnetic field, as shown in Fig 3(b), the V_{ANE} distribution changes, and the value becomes always positive. These results indicate that the octupole domains exhibit a remanent state along the wire-width direction (+y direction). However, the V_{ANE} signal is inhomogeneous, reflecting the presence of the grains with tilted Kagome planes about the x axis, consistent with the broad peak of (002) in Fig. 1(c), i.e., some grains with not-well-oriented kagome planes. Using a typical value of $V_{\text{ANE}} \sim 180$ nV in Figs. 3(d) and the simulated value of $\nabla_z T^L \sim 4 \times 10^6$ K/m, we obtained $S_{\text{ANE}} \sim 0.27$ $\mu\text{V}/\text{K}$. This value is greater than the estimation by the conventional method shown in Fig. 1(d) (0.18 $\mu\text{V}/\text{K}$), but close to the reported one in the single crystal Mn_3Sn (~ 0.3 $\mu\text{V}/\text{K}$) [39,42]. The nonuniform ANE distribution per grain explains this tendency: Some grains do not fully contribute to the ANE, probably due to their tilted Kagome planes, which decreases the thermoelectric efficiency from the intrinsic one. Using a typical value of $|V_{\text{SE}}^L| \sim 200$ nV and Eq. (3), we obtain $(S_{xx}^{(A)} - S_{xx}^{(B)}) \sim 0.17$ $\mu\text{V}/\text{K}$. As we have discussed before, due to the insufficient resolution, this value must be averaged across several grains, but the order of magnitude is consistent with the previous report, in which the S_{xx} along $[2\bar{1}\bar{1}0]$ and $[01\bar{1}0]$ differ by 0.7 $\mu\text{V}/\text{K}$ [38].

We observed the local anomalous Nernst effect in a (0001)-textured Mn_3Sn nanowire using the tip-contact-induced temperature gradient with 80 nm spatial resolution. Not like the magnetic imaging by the stray field measurement, our approach directly maps the distribution of the cluster magnetic octupole moments in Mn_3Sn . We visualized the octupole domains in the initial and remanent states in a nanowire, which is crucial information for the integration of Mn_3Sn . Our work provides a solid methodology to investigate the magnetic structures of the antiferromagnetic Weyl semimetal.

This work was partially supported by CREST (Grant No. JPMJCR18T3) from JST, JST-Mirai Program (Grant No. JPMJMI20A1), JSPS KAKENHI Grant-in-Aid for Scientific Research(C) (Grants No. 23K04579), and Steel Foundation for Environmental Protection Technology.

*Corresponding author: h_isshiki@issp.u-tokyo.ac.jp

- [1] S. Nakatsuji, N. Kiyohara, and T. Higo, Large anomalous Hall effect in a non-collinear antiferromagnet at room temperature, *Nature (London)* **527**, 212 (2015).
- [2] N. Kiyohara, T. Tomita, and S. Nakatsuji, Giant anomalous Hall effect in the chiral antiferromagnet Mn_3Ge , *Phys. Rev. Appl.* **5**, 064009 (2016).
- [3] A. K. Nayak *et al.*, Large anomalous Hall effect driven by a nonvanishing Berry curvature in the noncollinear antiferromagnet Mn_3Ge , *Sci. Adv.* **2**, e150187 (2016).
- [4] T. Chen *et al.*, Anomalous transport due to Weyl fermions in the chiral antiferromagnets Mn_3X , $\text{X} = \text{Sn}, \text{Ge}$, *Nat. Commun.* **12**, 572 (2021).
- [5] M.-T. Suzuki, T. Koretsune, M. Ochi, and R. Arita, Cluster multipole theory for anomalous Hall effect in antiferromagnets, *Phys. Rev. B* **95**, 094406 (2017).
- [6] N. Nagaosa, J. Sinova, S. Onoda, A. H. MacDonald, and N. P. Ong, Anomalous Hall effect, *Rev. Mod. Phys.* **82**, 1539 (2010).
- [7] D. Xiao, M.-C. Chang, and Q. Niu, Berry phase effects on electronic properties, *Rev. Mod. Phys.* **82**, 1959 (2010).
- [8] S. Nakatsuji and R. Arita, Topological magnets: Functions based on Berry phase and multipoles, *Annu. Rev. Condens. Matter Phys.* **13**, 119 (2022).
- [9] T. Higo, Y. Li, K. Kondou, D. Qu, M. Ikhlas, R. Uesugi, D. Nishio-Hamane, C. L. Chien, Y. Otani, and S. Nakatsuji, Omnidirectional control of large electrical output in a topological antiferromagnet, *Adv. Funct. Mater.* **31**, 2008971 (2021).
- [10] Y. Sakuraba, K. Hasegawa, M. Mizuguchi, T. Kubota, S. Mizukami, T. Miyazaki, and K. Takanashi, Anomalous Nernst effect in L10-FePt/MnGa thermopiles for new thermoelectric applications, *Appl. Phys. Express* **6**, 033003 (2013).
- [11] W. Zhou and Y. Sakuraba, Heat flux sensing by anomalous Nernst effect in Fe-Al thin films on a flexible substrate, *Appl. Phys. Express* **13**, 043001 (2020).
- [12] H. Tanaka, T. Higo, R. Uesugi, K. Yamagata, Y. Nakanishi, H. Machinaga, and S. Nakatsuji, Roll-to-roll printing of anomalous Nernst thermopile for direct sensing of perpendicular heat flux, *Adv. Mater.* **35**, 2303416 (2023).
- [13] X. Li, Z. Zhu, and K. Behnia, A monomaterial Nernst thermopile with hermaphroditic legs, *Adv. Mater.* **33**, 1 (2021).
- [14] N. Budai, H. Isshiki, R. Uesugi, Z. Zhu, T. Higo, S. Nakatsuji, and Y. Otani, High-resolution magnetic imaging by mapping the locally induced anomalous Nernst effect using atomic force microscopy, *Appl. Phys. Lett.* **122**, 102401 (2023).
- [15] H. Isshiki, N. Budai, and Y. Otani, Magneto-thermoelectric effects mapping using tip-induced temperature gradient in atomic force microscopy, *Front. Phys.* **11**, 1 (2023).
- [16] A. Sola, C. Barton, V. Basso, C. Dubs, M. Pasquale, and O. Kazakova, Local spin Seebeck imaging with a scanning thermal probe, *Phys. Rev. Appl.* **14**, 034056 (2020).
- [17] R. Puttock, C. Barton, E. Saugar, P. Klapetek, A. Fernández-Scarioni, P. Freitas, H. W. Schumacher, T. Ostler, O. Chubykalo-Fesenko, and O. Kazakova, Local thermoelectric response from a single Néel domain wall, *Sci. Adv.* **8**, eadc9798 (2022).
- [18] G. Q. Yan *et al.*, Quantum sensing and imaging of spin-orbit-torque-driven spin dynamics in the non-collinear antiferromagnet Mn_3Sn , *Adv. Mater.* **34**, 2200327 (2022).
- [19] S. Li, M. Huang, H. Lu, N. J. McLaughlin, Y. Xiao, J. Zhou, E. E. Fullerton, H. Chen, H. Wang, and C. R. Du, Nanoscale magnetic domains in polycrystalline Mn_3Sn films imaged by a scanning single-spin magnetometer, *Nano Lett.* **23**, 5326 (2023).
- [20] H. Reichlova *et al.*, Imaging and writing magnetic domains in the non-collinear antiferromagnet Mn_3Sn , *Nat. Commun.* **10**, 5459 (2019).

- [21] F. Johnson *et al.*, Identifying the octupole antiferromagnetic domain orientation in Mn_3NiN by scanning anomalous Nernst effect microscopy, *Appl. Phys. Lett.* **120**, 232402 (2022).
- [22] T. Higo *et al.*, Large magneto-optical Kerr effect and imaging of magnetic octupole domains in an antiferromagnetic metal, *Nat. Photonics* **12**, 73 (2018).
- [23] M. Wu, H. Isshiki, T. Chen, T. Higo, S. Nakatsuji, and Y. Otani, Magneto-optical Kerr effect in a non-collinear antiferromagnet Mn_3Ge , *Appl. Phys. Lett.* **116**, 132408 (2020).
- [24] T. Uchimura *et al.*, Observation of domain structure in non-collinear antiferromagnetic Mn_3Sn thin films by magneto-optical Kerr effect, *Appl. Phys. Lett.* **120**, 172405 (2022).
- [25] P. J. Brown, V. Nunez, F. Tasset, J. B. Forsyth, and P. Radhakrishna, Determination of the magnetic structure of Mn_3Sn using generalized neutron polarization analysis, *J. Phys. Condens. Matter* **2**, 9409 (1990).
- [26] C. Bippes, P. Frederix, P. Werten, and D. Yablon, CoreAFM: Research-grade AFM platform with application modularity, *Microsc. Today* **25**, 20 (2017).
- [27] A. Sakai *et al.*, Iron-based binary ferromagnets for transverse thermoelectric conversion, *Nature (London)* **581**, 53 (2020).
- [28] L. Leiva, S. Granville, Y. Zhang, S. Dushenko, E. Shigematsu, R. Ohshima, Y. Ando, and M. Shiraishi, Efficient room-temperature magnetization direction detection by means of the enhanced anomalous Nernst effect in a Weyl ferromagnet, *Phys. Rev. Mater.* **6**, 064201 (2022).
- [29] H. Tsai *et al.*, Electrical manipulation of a topological antiferromagnetic state, *Nature (London)* **580**, 608 (2020).
- [30] A. von Bieren, F. Brandl, D. Grundler, and J.-P. Ansermet, Space- and time-resolved Seebeck and Nernst voltages in laser-heated permalloy/gold microstructures, *Appl. Phys. Lett.* **102**, 052408 (2013).
- [31] A. Harzheim *et al.*, Geometrically enhanced thermoelectric effects in graphene nanoconstrictions, *Nano Lett.* **18**, 7719 (2018).
- [32] See Supplemental Material at <http://link.aps.org/supplemental/10.1103/PhysRevLett.132.216702> for thermoelectric voltage mapping on another Mn_3Sn device.
- [33] COMSOL Multiphysics® v. 6.1. www.comsol.com. COMSOL AB, Stockholm, Sweden. (n.d.).
- [34] A. Majumdar, Scanning thermal microscopy, *Annu. Rev. Mater. Sci.* **29**, 505 (1999).
- [35] S. Gomès, A. Assy, and P. O. Chapuis, Scanning thermal microscopy: A review, *Phys. Status Solidi* **212**, 477 (2015).
- [36] Y. Zhang, W. Zhu, F. Hui, M. Lanza, T. Borca-Tasciuc, and M. Muñoz Rojo, A review on principles and applications of scanning thermal microscopy (SThM), *Adv. Funct. Mater.* **30**, 1900892 (2020).
- [37] S. Lefèvre, S. Volz, and P. O. Chapuis, Nanoscale heat transfer at contact between a hot tip and a substrate, *Int. J. Heat Mass Transfer* **49**, 251 (2006).
- [38] T. Tomita, M. Ikhlas, and S. Nakatsuji, Large Nernst effect and thermodynamics properties in Weyl antiferromagnet, *J. Phys. Soc. Jpn.* **30**, 011009 (2020).
- [39] H. Narita, M. Ikhlas, M. Kimata, A. A. Nugroho, S. Nakatsuji, and Y. Otani, Anomalous Nernst effect in a microfabricated thermoelectric element made of chiral antiferromagnet Mn_3Sn , *Appl. Phys. Lett.* **111**, 202404 (2017).
- [40] H. R. Shanks, P. D. Maycock, P. H. Sidles, and G. C. Danielson, Thermal conductivity of silicon from 300 to 1400 °K, *Phys. Rev.* **130**, 1743 (1963).
- [41] W. Zhu, G. Zheng, S. Cao, and H. He, Thermal conductivity of amorphous SiO_2 thin film: A molecular dynamics study, *Sci. Rep.* **8**, 10537 (2018).
- [42] M. Ikhlas, T. Tomita, T. Koretsune, M.-T. Suzuki, D. Nishio-Hamane, R. Arita, Y. Otani, and S. Nakatsuji, Large anomalous Nernst effect at room temperature in a chiral antiferromagnet, *Nat. Phys.* **13**, 1085 (2017).